Far-field optical path noise coupled with the pointing jitter in the space measurement of gravitational waves

Ya Zhao,[1,2] Jia Shen,[2,3] Chao Fang,[1,*] Zhi Wang,[1,4] Ruihong Gao,[2,3] and Wei Sha[1]

[1]*Changchun Institute of Optics, Fine Mechanics and Physics Chinese Academic of Sciences, Changchun 130033, China*
[2]*University of Chinese Academy of Sciences, Beijing 100039, China*
[3]*Institute of Mechanics, Chinese Academy of Sciences, Beijing 100190, China*
[4]*e-mail: wz070611@126.com*
Corresponding author: fangchao@ciomp.ac.cn

Space-based gravitational wave detection programs, like the Laser Interferometer Space Antenna or the Taiji program, aim to detect gravitational waves in space with interferometric arms of millions of kilometers. In the process of far-field propagation, the exit wavefront error of the transmitting telescope will couple with the unavoidable pointing between two spacecraft to generate an optical path noise. In this paper, we firstly build a comprehensive theoretical model concerning the effect of 3rd ∼7th aberrations on this coupling and compare the coupling coefficients of different aberrations. Then, we use this model to analyze the far-field optical path noise of the exit wavefront of a built prototype telescope for the Taiji program. Finally, we take advantage of the Monte Carlo algorithm of the model for investigating the effect of the different wavefront qualities on optical path noise. The results can provide meaningful guidance for the construction of the subsequent telescope. © 2021 Optical Society of America

https://doi.org/10.1364/AO.405467

1. INTRODUCTION

In the space-borne and long-baseline laser interferometers such as the Laser Interferometer Space Antenna (LISA) and the Taiji program, there are three spacecraft (SC) forming an equilateral triangle with three million kilometers [1–3]. Each SC has two telescopes that collimate and expand the 1064 nm beam from the local optical bench and send it to a distant SC. As shown in Fig. 1, the interference arm length of the Taiji program is three million kilometers, and the telescope is a four-mirror Schiefspiegler system with 80 magnification and a diameter of the primary mirror of 400 mm [4]. Because of unavoidable manufacture and adjustment errors in the optical system, the wavefront at the exit pupil of the telescope will distort, which leads to the far-field wavefront deviating from the spherical wave. Consequently, the situation will combine with the pointing jitter to generate a phase noise. In order to successfully detect gravitational waves, the measurement noise of the detectors needs to meet $1\mathrm{pm}/\sqrt{\mathrm{Hz}}$ within the frequency band from 0.1 mHz to 1 Hz [5,6]. This ultra-low noise level has tight demands on the wavefront quality of the telescope.

Waluschka did numerical and ray tracing to analyze the effect of the wavefront error on the phase noise of the received beam of the distant SC [7–9]. Bender and Sasso *et al.* analytically

investigated the phase noise of the far-field wavefront induced by primary aberrations [10–12]. While Bender and Sasso *et al.* have derived analytical expressions of the far-field phase noise and focused on the effect of Seidel aberrations, it is shown that there are some higher-order aberrations existing in the exit pupil wavefront in the cases of thermal–structural–optical integrated analysis [4] and actual engineering implementation [13] of the telescope. Based on the analytic methods of Bender and Sasso, a theoretical model is firstly built for calculating the far-field phase noise produced by the coupling between the third to the seventh-order aberrations and the pointing jitter. Meanwhile, two coefficient matrices are obtained to analyze and compare the influences of different kinds of aberrations on the coupling. Next, using this theoretical model, the far-field phase noise of the completed prototype of the Taiji telescope is investigated, and the optimal pointing angle that causes the far-field optical path noise to be null is obtained. Finally, we use the Monte Carlo algorithm to analyze the influence of the wavefront with different qualities on the far-field phase noise. The results can provide a theoretical basis for the requirements of the exiting pupil wavefront quality of the subsequent telescope construction.
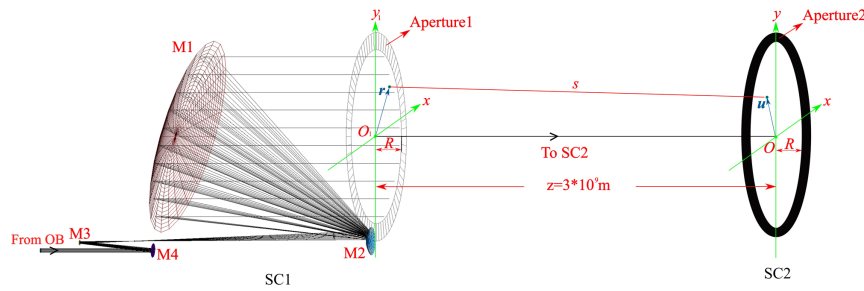
Fig. 1. Simplified diagram shows the process where the small beam from the optical bench (OB) is expanded to be a big Gaussian beam after passing the telescope and then traveling three million kilometers in free space to the remote SC2. $r = \{x_1, y_1\}$ and $u = \{x, y\}$ are the position vectors in the transmitting aperture and the receiving aperture, respectively. s is the distance from point r to point u. The primary, secondary, tertiary, and quaternary mirrors of the telescope are referred to as M1, M2, M3, and M4, respectively.

2. OPTICAL MODEL

A. Diffractional Transmission

The basic formula used is Kirchhoff's scalar formula [14]:

$$E(u) = \frac{e^{ikz}}{i\lambda z} e^{\frac{iku}{2z}} \int_A E_0(r) e^{ik(u \cdot r/z + \delta_W(r))} dr, \tag{1}$$

where $E_0(r)$ is the complex amplitude of the exit pupil of the local telescope. $\delta_W(r)$ is the wavefront error. $E(u)$ is the complex amplitude of the far-field wavefront clipped by the aperture of SC2. A represents the telescope aperture with the radius R. k is the wavenumber. After three million kilometers of propagation, the far-field beam is expanded into an Airy disk with the radius of 20 km. The extreme value of the factor $u \cdot r/z$ is about ± 13.3 pm, which is very small compared with the 10 nm scale factor $\delta_W(r)$. Therefore, we can use the on-axis amplitude ($u = 0$) to represent the whole received field of the receiving aperture. One of the important functions of the telescope is to expand the small Gaussian beam from the optical bench into a large Gaussian beam to reduce the divergence of beam energy. Therefore, we set $E_0(r) = e^{-r^2/\omega^2}$, where ω is the waist size of the exit beam. Omitting the factor $e^{ikz}/i\lambda z$ independent of the pointing jitter, the amplitude of the O point $E(0)$ is

$$E(0) = E_R + i * E_I, \tag{2}$$

where E_R, E_I defined in Eqs. (3) and (4) are the real and imaginary parts of $E(0)$, respectively. The range of the wavefront error $\delta_W(r)$ discussed in this paper is less than $\lambda/10$. So, based on computational accuracy, we use the approximations of the Taylor expansion of E_R and E_I as follows:

$$E_R = \int_A e^{-r^2/\omega^2} \cos(k\delta_W) dr$$

$$\approx \int_A e^{-r^2/\omega^2} dr - \frac{1}{2} \int_A e^{-r^2/\omega^2} k^2 \delta_W^2 dr, \tag{3}$$

$$E_I = \int_A e^{-r^2/\omega^2} \sin(k\delta_W) dr$$

$$\approx \int_A e^{-r^2/\omega^2} k\delta_W dr - \frac{1}{6} \int_A e^{-r^2/\omega^2} k^3 \delta_W^3 dr. \tag{4}$$

We define a_n as

$$a_n = \frac{1}{n!} \int_A e^{-r^2/\omega^2} (k\delta_W(r))^n dr. \tag{5}$$

Referencing the analytical approximation of [11], we can take the argument of Eq. (2) to get the phase error ϕ (the function arctan x is approximated as x, and the function $\frac{1}{1-x}$ is approximated as $1 + x$ in the approximation):

$$\phi = \arctan\left(\frac{E_I}{E_R}\right) \approx \frac{a_1 - a_3}{a_0 - a_2} \approx \frac{(a_1 - a_3)(a_0 + a_2)}{a_0^2}. \tag{6}$$

B. Model of the Wavefront Error

Zernike circle polynomials are used to form the wavefront error δ_W [15]:

$$Z_i(\rho, \theta) = \begin{cases} \sqrt{2(n+1)} R_n^m(\rho) \cos(m\theta) & i \text{ is even and } m \neq 0, \\ \sqrt{2(n+1)} R_n^m(\rho) \sin(m\theta) & i \text{ is odd and } m \neq 0, \\ \sqrt{n+1} R_n^0(\rho) & m = 0, \end{cases} \tag{7}$$

$$R_n^m(\rho) = \sum_{s=0}^{(n-m)/2} \frac{(-1)^s (n-s)!}{s!(\frac{n+m}{2} - s)!(\frac{n+m}{2} - s)!} \rho^{n-2s}, \tag{8}$$

where $R_n^m(\rho)$ of Eq. (8) is the radial polynomial, n and m are positive integers, and $n - m \geq 0$. $\rho = r/R$ is the normalized radial coordinate. The index i is a polynomial-ordering number and a function of n and m.

Here, the fringe Zernike polynomials, currently used by several vendors of interferometers, are chosen in the analysis. In order to fully characterize the manufacturing and adjustment errors of the optical systems, the first 25 terms of the fringe Zernike polynomials are used to fit the wavefront error (the piston term being omitted). The cosine and sine terms of the Zernike aberrations ($m \neq 0$) are combined to represent the magnitudes and orientations of these aberrations. For example, when both x and y Zernike tilts are used to present the wavefront tilt, the aberration may be written as the form

$$a_2 Z_2(\rho, \theta) + a_3 Z_3(\rho, \theta) = A_1^{\text{Ti}} \rho \cos(\theta - \theta_{\text{Ti}}), \tag{9}$$

showing a wavefront tilt of magnitude $A_1^{\text{Ti}} = 2\sqrt{a_2^2 + a_3^2}$ with an azimuth angle $\theta_{\text{Ti}} = \tan^{-1}(a_3/a_2)$, where a_i is the expansion coefficient before combination, and A_j^{aber} is the magnitude

Table 1.   Fourteen Zernike Aberrations Consisting of the First 25 Terms of Fringe Zernike Polynomials

i	n, m	j	$Z_j(\rho, \theta)$	Aberration Name
2,3	1, ±1	1	$\rho \cos(\theta - \theta_{Ti})$	Tilt
4	2,0	2	$\sqrt{3}(2\rho^2 - 1)$	Defocus
5,6	2, ±2	3	$\sqrt{6}\rho^2 \cos(2\theta - (\theta_{PA}))$	Primary astigmatism
7,8	3, ±1	4	$\sqrt{8}(3\rho^3 - 2\rho) \cos(\theta - (\theta_{PC}))$	Primary coma
9	4,0	5	$\sqrt{5}(6\rho^4 - 6\rho^2 + 1)$	Primary spherical
10,11	3, ±3	6	$\sqrt{8}\rho^3 \cos(3\theta - \theta_{PTR})$	Primary trefoil
12,13	4, ±2	7	$\sqrt{10}(4\rho^4 - 3\rho^2) \cos(\theta - \theta_{SA})$	Secondary astigmatism
14,15	5, ±1	8	$\sqrt{5}(10\rho^5 - 12\rho^3 + 3\rho) \cos(2\theta - \theta_{SC})$	Secondary coma
16	6, 0	9	$\sqrt{5}(20\rho^6 - 30\rho^4 + 12\rho^2 - 1)$	Secondary spherical
17,18	4, ±4	10	$\sqrt{5}\rho^4 \cos(4\theta - \theta_{PTE})$	Primary tetrafoil
19,20	5, ±3	11	$\sqrt{8}(5\rho^5 - 4\rho^3) \cos(3\theta - \theta_{STR})$	Secondary trefoil
21,22	6, ±2	12	$\sqrt{5}(15\rho^6 - 20\rho^4 + 6\rho^2) \cos(2\theta - \theta_{TA})$	Tertiary astigmatism
23,24	7, ±1	13	$\sqrt{5}(35\rho^7 - 60\rho^5 + 30\rho^3 - 4\rho) \cos(2\theta - \theta_{TC})$	Tertiary coma
25	8, 0	14	$\sqrt{5}(70\rho^8 - 140\rho^6 + 90\rho^4 - 20\rho^2 + 1)$	Tertiary spherical

of the aberration after combination (its subscript is the serial number j, and the superscript is the abbreviation of the corresponding aberration). Here, the effect of the pointing jitter α can be characterized by the wavefront tilt $\alpha = A_1^{Ti}/R$. The relationship between $Z_i(\rho, \theta)$ and $Z_i(\rho, \theta)$ ($i \neq 4, 9, 16, 25$) can be defined as

$$A_j^{aber} Z_j(\rho, \theta) = a_i Z_i(\rho, \theta) + a_{i+1} Z_{i+1}(\rho, \theta) \quad (i \neq 4, 9, 16, 25). \tag{10}$$

The complete orthonormal Zernike polynomials $Z_j(\rho, \theta)$ in polar coordinates are given in Table 1, where θ_{aber} presents an orientation angle of the corresponding aberration inclined with the x axis, and its subscript is the abbreviation of the corresponding aberration. As a result, the wavefront error can be presented as

$$\delta_W(\rho, \theta) = A_1^{Ti} \rho \cos(\theta - \theta_{Ti}) + \sum_{j=2}^{14} A_j^{aber} Z_j(\rho, \theta). \tag{11}$$

The aberration variance σ is given by

$$\sigma = \sum_j (A_j^{aber})^2, \tag{12}$$

where σ can be regarded as the root-mean-square (RMS) value of the wavefront error because the piston term is not included here.

C. Optical Path Noise Induced by the Pointing Jitter

Next, we carry out the symbolic calculations of the integration of Eqs. (5) and (6) by utilizing Mathematica [the Mathematica code is available in the supplementary material, as shown in Code 1, Ref. [16]]. Because we consider the dependence of the phase noise on the small pointing jitter, the terms unrelated and higher than the second order of A_1^{Ti} are omitted during simplification.

In order to get clear analytic expressions, we define aberration vector v_1 including the three coma terms (including defocus) and the two trefoil terms and aberration vector v_2 including the four spherical terms (including defocus), the three astigmatism terms, and the primary tetrafoil term, as shown in Eqs. (13) and

(14), respectively. Meanwhile, we define the coefficients B_1 and B_2 shown in Eqs. (15) and (16), respectively, where M1 and M2 are the 8×5 coefficients matrix and the 1×8 coefficients matrix, respectively:

$$v_1 \Rightarrow \left\{ A_4^{PC}, A_8^{SC}, A_{13}^{TC}, A_6^{PTR}, A_{11}^{STR} \right\}, \tag{13}$$

$$v_2 \Rightarrow \left\{ A_2^{DE}, A_5^{PS}, A_9^{SS}, A_{14}^{TS}, A_3^{PA}, A_7^{SA}, A_{12}^{TA}, A_{10}^{PTE} \right\}, \tag{14}$$

$$B_1 = v_1 * M_1 * v_2^T, \tag{15}$$

$$B_2 = v_2 * M_2^T. \tag{16}$$

As a result, the optical path error (OPE), through dividing the phase error ϕ by the wavenumber k, can be expressed as

$$\text{OPE} \approx B_1 * A_1^{Ti} + B_2 * (A_1^{Ti})^2. \tag{17}$$

Meanwhile, the sensitivity index δ_{OPE} as defined in Eq. (18), calculated by taking the derivatives of Eq. (17) with respect to α, characterize the sensitivity of OPE to the pointing jitter:

$$\delta_{OPE} \approx (B_1 + 2 * B_2 * A_1^{Ti}) * R. \tag{18}$$

The coefficient matrices M_1 and M_2 are the functions of the normalized radius $\omega_r = \omega/R$ and the cosine of the add and subtract combination between θ_{Ti} and θ_{aber}. As shown in Eqs. (19) and (20), $M_1(1, 1)$ and $M_1(4, 5)$ represent the coefficients of the factors $A_2^{DE} * A_4^{PC}$ and $A_3^{PA} * A_6^{PTR}$ in B_1, respectively. As shown in Eqs. (21) and (22), $M_2(1)$ and $M_2(5)$ represent the coefficients of the factors A_2^{DE} and A_3^{PA} in B_2, respectively. The complete expressions of all the elements in M_1 and M_2 are not shown here due to limited space. In order to compare the contributions of different aberration terms to OPE, we set the normalized radius $\omega_r = 1$, and the cosine terms are equal to one by setting θ_{Ti} and other θ_{aber} to zero. For convenience of comparison, we take the absolute value for specific coefficient matrices M_1 and M_2 and normalize them by dividing each element of the matrix by the largest element. Figure 2 shows that the higher the order of the aberration term is, the smaller the contribution of the aberration to OPE is in general. For
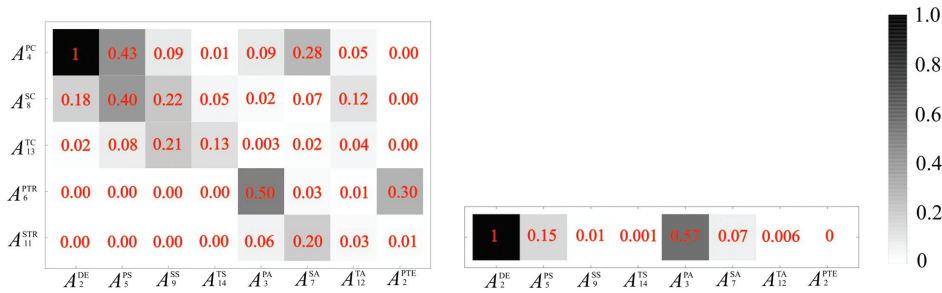
Fig. 2. (Left) Normalized M_1. (Right) Normalized M_2.

instance, in the matrix M_1, the maximum value of the columns corresponding to the four spherical aberration terms are 1, 0.43, 0.22, and 0.13, the maximum value of the columns corresponding to the three astigmatism terms are 0.5, 0.28, and 0.12, and the maximum value of the rows corresponding to the three coma terms are 1, 0.40, and 0.21. This characteristic is more obvious in M_2. We can also find that the contributions of the spherical aberration terms to OPE are generally greater than that of the astigmatism terms, and both of them are coupled with the coma terms, but there is no coupling between them:

$$M_1(1,\,1) = \frac{1}{8\sqrt{6}}k^2\operatorname{csch}^2\left(\frac{1}{2\omega_r^2}\right)\cos\left(\theta_{PC} - \theta_{Ti}\right) * \left(24\omega_r^6 + 2\omega_r^4 + 6\omega_r^2 + 6\omega_r^4\sinh\left(\frac{1}{\omega_r^2}\right) - 2\left(12\omega_r^6 + \omega_r^4\right)\cosh\left(\frac{1}{\omega_r^2}\right) + 1\right),$$

(19)

$$M_1(4,\,5) = -\frac{k^2\left(6\left(e^{\frac{1}{\omega_r^2}} - 1\right)\omega_r^6 - 6\omega_r^4 - 3\omega_r^2 - 1\right)\cos\left(\theta_{PTR} - \theta_{PA} - \theta_{Ti}\right)}{16\sqrt{3}\left(e^{\frac{1}{\omega_r^2}} - 1\right)},$$

(20)

$$M_2(1) = \frac{1}{8\sqrt{3}}k^2\left(\operatorname{csch}^2\left(\frac{1}{2\omega_r^2}\right) - 4\omega_r^4\right),$$

(21)

$$M_2(5) = -\frac{k^2\left(2\left(e^{\frac{1}{\omega_r^2}} - 1\right)\omega_r^4 - 2\omega_r^2 - 1\right)\cos\left(\theta_{PA} - 2\theta_{Ti}\right)}{8\sqrt{6}\left(e^{\frac{1}{\omega_r^2}} - 1\right)},$$

(22)

where

$$\operatorname{csch} = \frac{2}{e^x - e^{-x}}.$$

(23)

3. FAR-FIELD OPTICAL PATH PHASE OF THE PROTOTYPE TELESCOPE

Taking into account the stringent requirements of stray light ($\leq 10^{-10}$ in the science field of view) in the space-based interferometry system, the telescope adopts the off-axis four-mirror structure, which is an optimized Schiefspiegler system consisting of a parabolic primary mirror, a hyperbolic secondary mirror, and spherical tertiary and quaternary mirrors. Considering the verification of the key technologies of the Taiji program, a sub-scale prototype was constructed. Compared with the final mission parameters, the prototype has a primary clear aperture of 200 mm with a magnification of 40.

The built prototype implementation is shown on the left of Fig. 3. The materials used in the four mirrors and the supporting structure are silicon carbide (SiC) and the Invar alloy, respectively. The surface shapes of the four mirrors are shown on the right of Fig. 3. The RMS values of the four mirrors are about 16.4 nm, 24.8 nm, 11.5 nm, and 9.8 nm, respectively. The alignment strategy of the prototype telescope is that M1 is fixed as the benchmark, and the positions of M2, M3, and M4 are then adjusted iteratively to optimize the exit pupil wavefront.

As shown on the left of Fig. 4, the RMS value of the practical wavefront error of the built prototype is deteriorated to be 76 nm ($\lambda/14$), compared to the designed residual 3 nm of the prototype telescope, shown on the right of Fig. 4. The surface-shape errors of the four mirrors contribute about 33.5 nm calculated by the square root of the sum of the squares of the RMS values of the four mirrors. The remaining error comes from the adjustment error of the system.

Although the exit wavefront quality of the prototype telescope is not ideal, we can still use it as a sample. It is then decomposed as the Zernike spectrum shown in Table 2, which are taken into Eqs. (15) and (16) to calculate the corresponding coefficients B_1 and B_2 shown as Eqs. (24) and (25), respectively:

$$B_1 = 0.0284528\sin(\theta_{Ti}) - 0.000662576\cos(\theta_{Ti}),$$

(24)

$$B_2 = -121.54\sin^2(\theta_{Ti}) + 121.54\cos^2(\theta_{Ti})$$
$$- 90.4897\sin(\theta_{Ti})\cos(\theta_{Ti}) - 71.9551.$$

(25)

The corresponding OPE and sensitivity index δ_{OPE} at the receiving SC are shown in Fig. 5, as the function of the horizontal and vertical tilts α_x, α_y ($\omega = R = 100$ mm). The results
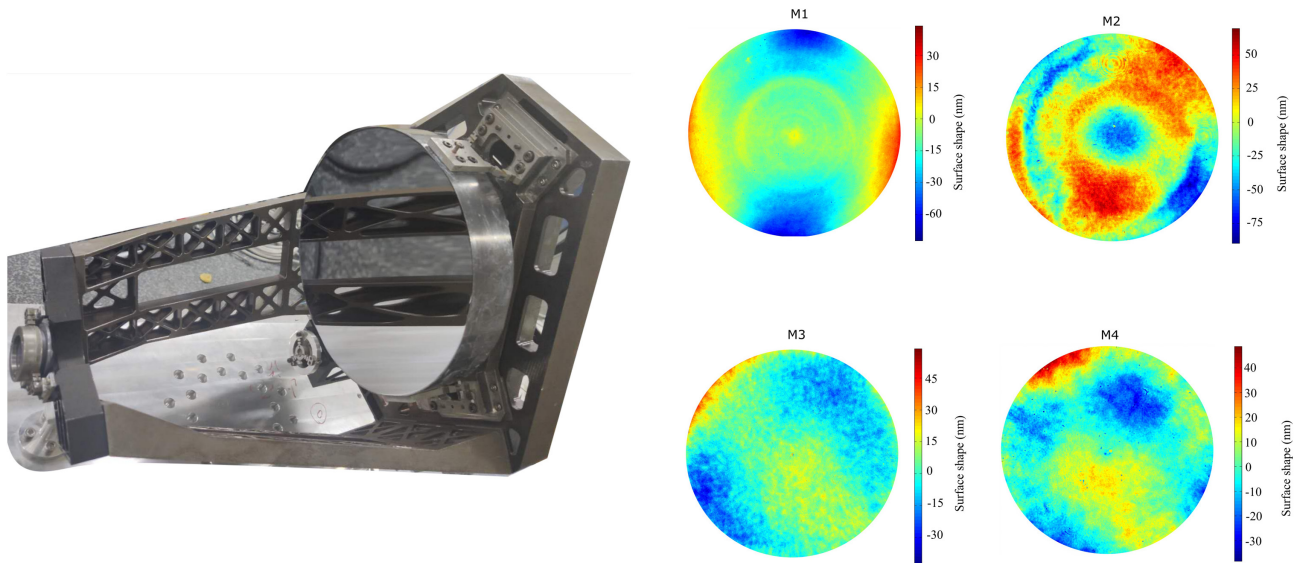
Fig. 3. (Left) Built model of the prototype telescope. It is worth noting that there are many weight reducing holes in the invar structures. (Right) Surface shape of the four mirrors used in the prototype telescope. The astigmatism and the coma are clearly seen in these pictures.
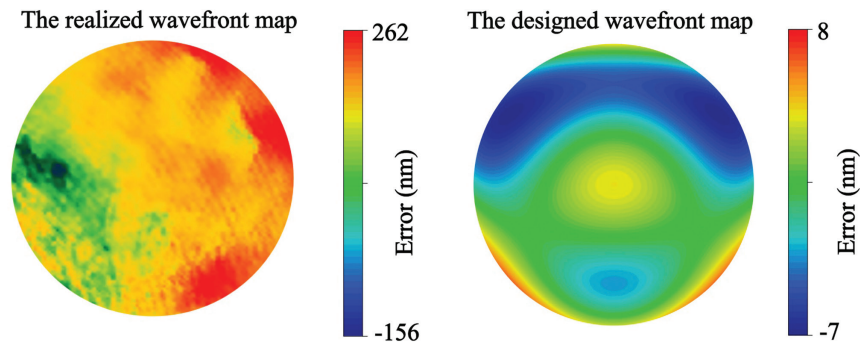

Fig. 4. (Left) Realized wavefront map of the aligned prototype telescope. (Right) Residual aberration of the ideal design of the prototype telescope.

Table 2.   Magnitude and Orientation of the Zernike Spectrum of the Exit Wavefront Error of the Prototype Telescope

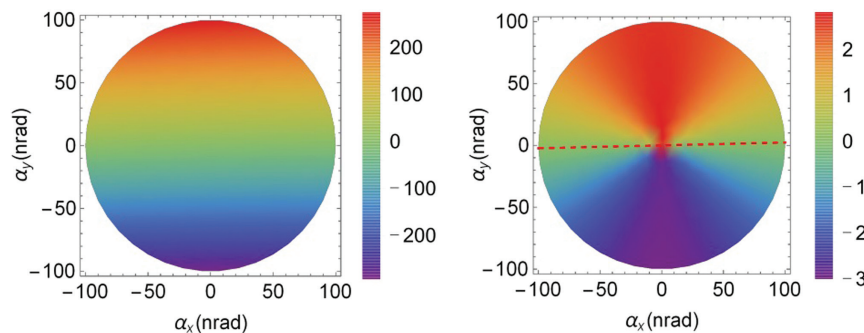| Mag/ori	A_2^{DE}	A_3^{PA}/θ_{PA}	A_4^{PC}/θ_{PC}	A_5^{PS}	A_6^{PTR}/θ_{PTR}	A_7^{SA}/θ_{SA}
nm/rad	26.6	23.8/2.62	44.9/4.6	47.2	22.3/0.95	18.4/1.06
A_8^{SC}/θ_{SC}	A_9^{SS}	$A_{10}^{PTE}/\theta_{PTE}$	$A_{11}^{STR}/\theta_{STR}$	A_{12}^{TA}/θ_{TA}	A_{13}^{TC}/θ_{TC}	A_{14}^{TS}
22.4/0.57	21.03	5.49/5.33	1.02/4.67	9.71/5.67	0.81/1.82	8.26

Fig. 5. (Left) Far-field OPE of the pupil wavefront of the prototype telescope with the range from −300 to 250 pm. (Right) Corresponding sensitivity index δ_{OPE} with the range from −3 to 2.5 pm/nrad. The red dotted curve indicates the positions with the zero value corresponding to the pointing direction θ_{00}^{Ti}.
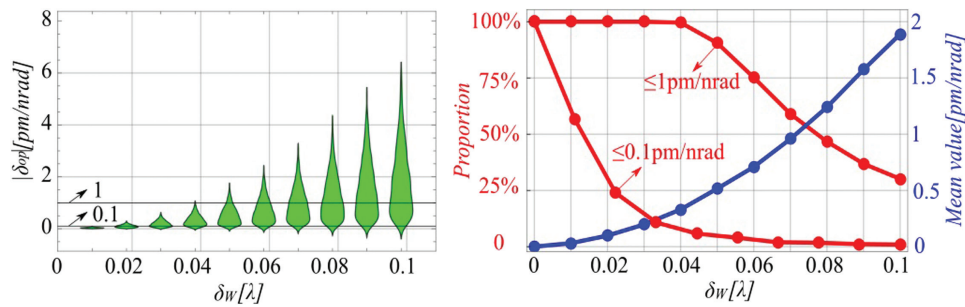
Fig. 6. In the range of $0 \sim \lambda/10$ and the step of $\lambda/100$ for δ_W. (Left) Sample distributions of δ_{OPE} versus δ_W. (Right) The mean values and the proportions (≤ 0.1 pm/nrad and ≤ 1 pm/nrad) of δ_{OPE} versus δ_W, the data points are linked into lines, respectively. The specific values are shown in Table 3.

show that the maximum sensitivity of the optical path noise to the pointing jitter within ± 100 nrad is about 3 pm/nrad. It is worth noting that the red dotted line indicating the null δ_{OPE} is almost a straight line. The reason is that compared with B_1, the term $2 * B_2 * A_1^{\mathrm{Ti}}$ is very small because of the small jitter range $\alpha = \pm 100$ nrad. As a result, the sensitivity index δ_{OPE} depends more on the direction of the jitter angle than its value, shown on the right of Fig. 5. We make Eq. (24) equal to zero to obtain pointing direction $\theta_{00}^{\mathrm{Ti}} = \arctan(0.023)$. It means that for the far field of the prototype telescope, the optical path noise induced by the pointing jitter can be null if the horizontal and vertical jitters satisfy $\alpha_y/\alpha_x = 0.023$. The reason the right side of Fig. 5 shows the non-zero sensitivity near the position of $\alpha_x = \alpha_y = 0$ is that the zero value of the optimal pointing direction $\theta_{00}^{\mathrm{Ti}}$ is covered by the non-zero value of other jitter directions because of the dramatic change in the jitter direction.

4. SIMULATION AND ANALYSIS

In order to provide guidance for the engineering implementations of the subsequent telescopes, it is necessary to predict the far-field optical path noise under different constraints of the exit wavefront error δ_W by adopting the Monte Carlo simulation for the analytical results of the previous section.

In the following analysis, we carry out the Monte Carlo algorithm to generate 10^4 groups of A_j^{aber} (expect A_1^{Ti}) and θ_{aber} (including θ_{Ti}), respectively, in the cases of 10 different

Table 3. Specific Mean Values, the Proportions (≤ 0.1 pm/nrad and ≤ 1 pm/nrad) and the Distribution Ranges of 10^4 Samples of δ_{OPE} for Every δ_W

$\delta_W[\lambda]$	Mean (pm/nrad)	Pro ($\leq$ 0.1 pm/nrad)	Pro ($\leq$ 1 pm/nrad)	Range (pm/nrad)
0.01	0.03	100%	100%	0–0.09
0.02	0.10	56.4%	100%	0–0.32
0.03	0.20	23.9%	100%	0–0.69
0.04	0.33	10.7%	99.6%	0–1.32
0.05	0.51	5.8%	90.5%	0–2.10
0.06	0.71	3.9%	75.2%	0–3.10
0.07	0.96	1.9%	59.0%	0–4.29
0.08	1.24	1.7%	46.7%	0–5.12
0.09	1.57	1.1%	36.8%	0–6.85
0.1	1.89	0.9%	30.1%	0–7.54

constraints of σ, which are in the range of $0 \sim \lambda/10$ with the step of $\lambda/100$. After obtaining the function δ_{OPE} depending on the wavefront jitter A_1^{Ti} by substituting the parameter values of each group to Eq. (18), we maximize the absolute value $|\delta_{\mathrm{OPE}}|$ by optimizing the pointing jitter $\alpha = A_{\mathrm{Ti}}/R$ in the range of ± 100 nrad to consider the worst situation for every sample.

Figure 6 illustrates the simulation results, and Table 3 shows the mean values, the proportions (≤ 0.1 pm/nrad and ≤ 1 pm/nrad), and the distribution ranges of $|\delta_{\mathrm{OPE}}|$ for every δ_W. The results obviously show that the values and distribution ranges of $|\delta_{\mathrm{OPE}}|$ will increase with the increase of δ_W in general.

5. CONCLUSION

In this paper, we firstly construct the theoretical optical model of the far-field optical path noise of the laser beam transmitting three million kilometers with the wavefront aberrations. Then, taking into account the first 25 terms of the fringe Zernike polynomials for constituting the wavefront aberrations, we obtain the expressions of Eqs. (17) and (18) to calculate the optical path noise and compare the contribution of different aberrations of noise by the coefficient matrices. The results show that higher-order aberration terms contribute less to the optical path noise, and the influence of the spherical aberration terms on the noise are generally greater than the astigmatism terms. Next, we use these analytical expressions to investigate the far-field optical path noise of the prototype telescope with the $\lambda/14$ (RMS) exit wavefront error. The result shows that the corresponding sensitivity to the pointing jitter in the range of ± 100 nrad is $-3 - 2.5$ pm/nrad, and the sensitivity depends more on the direction of the jitter angle than its value in a small jitter range. We obtain an optimal pointing direction of 0.023 rad, which leads to the zero sensitivity.

Finally, we use the analytical expression to implement the Monte Carlo algorithm in the case of the arbitrary wavefront aberrations. Considering Murphy's Law, we optimize the pointing tilt angle in the range of ± 100 nrad in order to take the maximum sensitivity of the optical path noise to the pointing jitter. The results show that if the required sensitivity to the beam jitter is less than 1 pm/$\sqrt{\mathrm{Hz}}$, the RMS of the wavefront error needs to be less than $\lambda/50$ with a noise spectral density of 10 nrad/$\sqrt{\mathrm{Hz}}$ of the pointing jitter. If the noise spectral density of the pointing jitter can be controlled to be 1 nrad/$\sqrt{\mathrm{Hz}}$, the RMS of the wavefront error can be relaxed to be 0.07λ.

REFERENCES

1. K. Danzmann, and the LISA Study Team, "LISA: laser interferometer space antenna for gravitational wave measurements," Class. Quantum Gravity **13**, A247–A250 (1996).
2. Z. Luo, Z. Guo, G. Jin, Y. Wu, and W. Hu, "A brief analysis to Taiji: science and technology," Results Phys. **16**, 102918 (2020).
3. Y. Dong, H. Liu, Z. Luo, Y. Li, and G. Jin, "A comprehensive simulation of weak-light phase-locking for space-borne gravitational wave antenna," Sci. China Technol. Sci. **59**, 730–737 (2016).
4. Z. Wang, T. Yu, Y. Zhao, Z. Luo, W. Sha, C. Fang, Y. Wang, S. Wang, K. Qi, Y. Wang, and X. Xu, "Research on telescope TTL coupling noise in intersatellite laser interferometry," Photon. Sens. **10**, 265–274 (2020).
5. M. Chwalla, K. Danzmann, G. F. Barranco, E. Fitzsimons, O. Gerberding, G. Heinzel, C. J. Killow, M. Lieser, M. Perreur-Lloyd, D. I. Robertson, S. Schuster, T. S. Schwarze, M. Tröbs, H. Ward, and M. Zwetz, "Design and construction of an optical test bed for LISA imaging systems and tilt-to-length coupling," Class. Quantum Gravity **33**, 245015 (2016).
6. A. Sutton, K. McKenzie, B. Ware, and D. A. Shaddock, "Laser ranging and communications for LISA," Opt. Express **18**, 20759–20773 (2010).
7. M. Papalexandris and E. Waluschka, "Numerical phase front propagation for a large-baseline space interferometer," Opt. Eng. **42**, 1029–1037 (2003).
8. E. Waluschka, "LISA far-field phase patterns," Proc. SPIE **3779**, 31–39 (1999).
9. E. Waluschka and M. V. Papalexandris, "LISA telescope sensitivity analysis," Proc. SPIE **4767**, 114–122 (2002).
10. P. L. Bender, "Wavefront distortion and beam pointing for LISA," Class. Quantum Gravity **22**, S339–S346 (2005).
11. C. P. Sasso, G. Mana, and S. Mottini, "Coupling of wavefront errors and jitter in the LISA interferometer: far-field propagation," Class. Quantum Gravity **35**, 185013 (2018).
12. C. P. Sasso, G. Mana, and S. Mottini, "Telescope jitters and phase noise in the LISA interferometer," Opt. Express **27**, 16855–16870 (2019).
13. S. R. Sankar and J. C. Livas, "Optical alignment and wavefront error demonstration of a prototype LISA telescope," Class. Quantum Gravity **37**, 065005 (2020).
14. Y. Hu, Z. Wang, X. Wang, S. Ji, C. Zhang, J. Li, W. Zhu, D. Wu, and J. Chu, "Efficient full-path optical calculation of scalar and vector diffraction using the Bluestein method," Light: Sci. Appl. **9**, 119 (2020).
15. D. Malacara, *Optical Shop Testing* (Wiley, 2007).
16. Y. Zhao, "The Mathematica codes for the symbolic calculations and the analysis," figshare, 2020, https://doi.org/10.6084/m9.figshare.12800657.